34

STM-Based Techniques Combined with Optics

Hidemi Shigekawa
University of Tsukuba

Osamu Takeuchi
University of Tsukuba

Yasuhiko Terada
University of Tsukuba

Shoji Yoshida
University of Tsukuba

34.1 Introduction 34-1
34.2 Specific Issues in Techniques Combined with Optical Technologies 34-2
Thermal Expansion Effect • Photoelectron Emission • Displacement Current • Tip Shape Effect • Stray Light
34.3 Probing Carrier Dynamics in Semiconductors 34-4
Tip-Induced Band Bending and Surface Photovoltage • Light-Modulated Scanning Tunneling Spectroscopy • Femtosecond Time-Resolved STM
34.4 Other Techniques 34-10
With Optical Manipulation • Optical Modulation of Bias Voltage • With Variation in Photoexcitation Wavelength • Spin-Polarized Excitation • With Synchrotron Radiation • STM-Induced Light Emission • With Near-Field Optics • Fabrication
34.5 Summary 34-14
References 34-15

34.1 Introduction

Through the efforts of the researchers devoted over the last decade, unprecedented advances have been made in developing nanoscale materials and devices with novel functions. Through nanoscale fabrications, elemental blocks of various characteristics are integrated and organized on a designed stage to produce desired or new functions in a system on the macroscopic scale (Figure 34.1). However, with the reduction in the size of structures, differences in electronic properties, for example, that due to the structural nonuniformity in each element, has an even more crucial effect on macroscopic functions.

Figure 34.2a and b shows a scanning tunneling microscopy (STM) image of an Si nanoparticle of ~3 nm diameter on a graphite surface and the cross sections of the same region obtained at different bias voltages. Inhomogeneous structures are observed in the cross sections. Since STM provides information on the electronic structures at the observed bias voltage (Wiesendanger 1994, Sakurai and Watanabe 1999), the result indicates the presence of complex electronic structures even at the single-molecular level. The miniaturization of semiconductor devices into a 10 nm scale brings about another example. Local structures, such as atomic defects and dopant materials, inevitably affect and govern the characteristic properties of macroscopic functions (Figure 34.3).

Therefore, the direct observation of the characteristic properties of nanostructures, which provides us with the basis for the macroscopic analysis of results, is of great importance. Thus, for further advancement in the development of new functional materials and devices, a method of exploring the transient dynamics of the local quantum functions in organized small structures is desired.

In STM, a sharp tip is placed close to a target material (Figure 34.4), and information on the region underneath the STM tip is obtained using a tunneling current. In general, the local density of states of the material under an equilibrium condition is measured with a certain bias voltage applied between the STM tip and the sample. However, when some perturbation is added from outside, we can analyze the dynamics of the system by observing its responses to the changes in conditions.

When optical modulation is adopted, the dynamics of transient electronic states and structural changes induced in materials by photoexcitation, providing a variety in functional properties of materials and devices (Figure 34.5), may be analyzed by STM. Therefore, in order to take full advantage of functions of materials in miniaturized devices, it is of great importance to develop new microscopy techniques that enable us to study photoinduced phenomena on the nanoscale.

This chapter describes the STM and related techniques combined with optical technologies in detail. Section 34.2 presents the specific issues brought by the combination with optical technologies and the methods of treating them. Section 34.3 shows the basic principles and techniques for probing the carrier dynamics

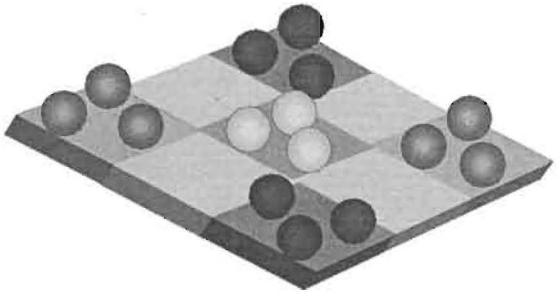

FIGURE 34.1 Schematic model of nanoscale system.

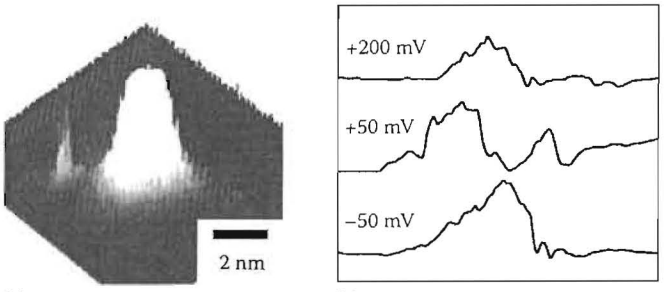

FIGURE 34.2 (a) STM current image of Si nanoparticle on graphite surface and (b) cross sections of same region obtained at different bias voltages.

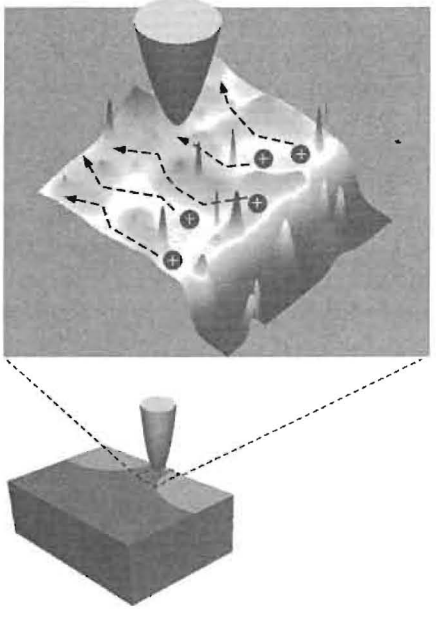

FIGURE 34.3 Schematic of carrier dynamics modulated in nanoscale potential landscape.

of nanoscale semiconductor structures using laser-combined STM. In Section 34.4, some other cases are introduced. Although it is difficult to cover all the related topics, the materials discussed in this chapter are presented in a form that is instructive to non-specialists as well as specialists. This makes it possible to develop the ability of handling the issues we face in the measurement

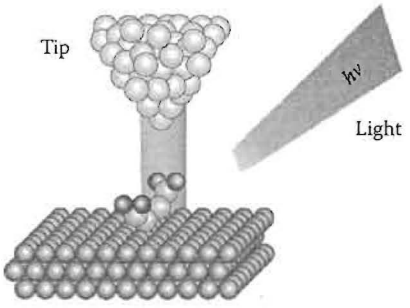

FIGURE 34.4 STM setup with additional modulation from outside (light modulation in this case).

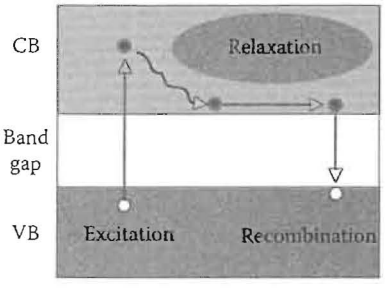

FIGURE 34.5 An example presenting excitation and relaxation processes for photoexcited carriers in semiconductor.

using the new microscopy techniques. With ingenuity, a new method can be developed.

34.2 Specific Issues in Techniques Combined with Optical Technologies

A super-band gap photoillumination of a semiconductor sample, for example, produces electron–hole pairs, inducing a photocurrent and the surface photovoltage (SPV) effect in STM measurement, which can be probed as a signal and used for analyzing the carrier dynamics. However, since optical excitation produces other various phenomena, we should carefully develop experimental and analytical methods to obtain meaningful information using the new STM and related techniques. Typical issues are discussed in this section.

34.2.1 Thermal Expansion Effect

The most obvious and critical issue is the thermal expansion of the STM tip and sample, due to the heat brought by photoillumination. In most cases, the effect of tip expansion is dominant because of the shape of the tip. When the light intensity is constant, the temperature and thereby the length of the STM tip gradually increase until they reach equilibrium under illumination. Once an equilibrium condition is achieved, STM observation can be performed stably. In contrast, when the light intensity oscillates, the tip repeatedly expands and shrinks. Since the tunneling current is extremely sensitive to the tip-sample distance,

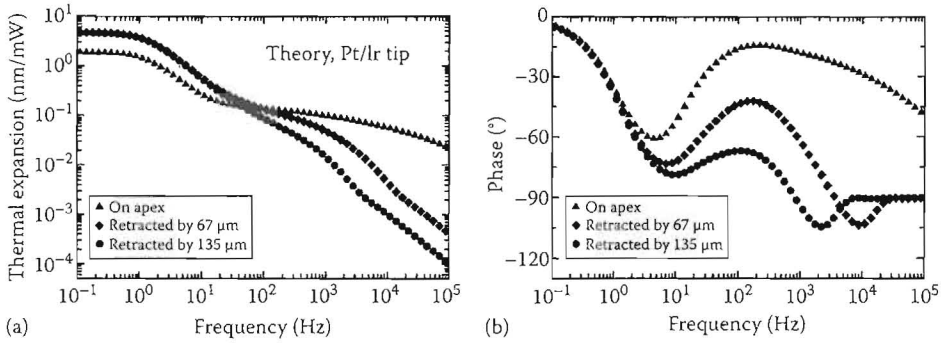

FIGURE 34.6 (a) Chopping frequency dependence of thermal expansion effect on Pt/Ir STM tip (theory). (b) Three series correspond to the results obtained at three different illumination spot positions. (From Grafström, S., *J. Appl. Phys.*, 83, 3453, 1998. With permission.)

this phenomenon affects the STM measurement. In the worst-case scenario, the tip crashes into the sample surface.

The modulation of the light intensity is caused, for example, by the use of an optical chopper or a train of a pulse laser, and the noise due to the fluctuation in the light source. To reduce the effect of heat without decreasing the light density, it is important to reduce the light spot size. When pulsed illumination is used, increasing its frequency is effective for reducing the effect of heat. As shown by the response characteristics of tip length against the chopping frequency of photoillumination in Figure 34.6, the thermal expansion effect is smaller at higher frequencies (Grafström 1998). However, note that the finite effect still exists even when the modulation frequency is as high as 100 kHz, which is already above the bandwidth of the STM tunnel current preamplifier. A superior method that is effective for the use of a short-pulse laser with STM is explained in Section 34.3.3.

34.2.2 Photoelectron Emission

Photoillumination with energy above the work function causes photoelectron emission. For a pulse laser with a high peak intensity, the multiple photon absorption effect may additionally cause photoemission even when the photon energy is below the gap energy. Thus, the photon energy and peak intensity must be chosen to suppress this effect (Jersch 1999). Since the tip-sample distance dependence of the photoelectron current is small, its effect on the measurement can be distinguished from the tunnel current by increasing the tip-sample separation up to ~10 nm, where the tunnel current significantly diminishes. The photoelectron current is smaller in air because the mean free path becomes shorter. The use of photocurrent is introduced in Section 34.4.5.

34.2.3 Displacement Current

Another possible source of the unfavorable current for the measurement of tunnel current is the displacement current from the stray capacitance at the tunnel junction. The nanoscale metal–insulator–semiconductor (MIS) junction, consisting of the STM tip, tunnel gap, and semiconductor sample (Figure 34.9 in Section 34.3.1), works as a capacitor that accumulates a certain amount of charge as a function of the applied bias voltage, similarly to the gate capacitor of a field effect transistor. When the gap is illuminated and the SPV is induced, the effective bias voltage changes, resulting in the flow of the displacement current from the capacitor. This current appears only when the light intensity changes.

The stray capacitance has a smaller dependence on the tip-sample distance, similarly to the photocurrent. Thus, this effect is also distinguished from the tunnel current by increasing the tip-sample separation up to ~10 nm.

Although the spatial resolution is limited to ~1 μm, the measurement of displacement current enabled the analysis of carrier dynamics in a semiconductor with the temporal resolution of ~10 ns (Hamers and Cahill 1991). An example for the use of the displacement current is shown in Section 34.4.3.

34.2.4 Tip Shape Effect

The shadowing of the photoillumination by the STM tip is an issue that must be considered. This effect can be reduced by STM tip sharpening. Figure 34.7 shows an example of a sharp tungsten tip electrochemically etched in NaOH solution (Williams 2008). Such a sharp tip has an apex with a curvature radius smaller than the optical wavelength. Thus, it does not drop its shadow on the sample surface. Its effect is rather scattering than shadowing, allowing us to illuminate the tunnel gap despite the existence of the STM tip.

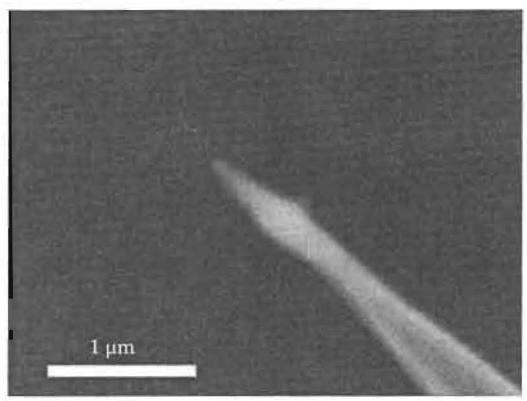

FIGURE 34.7 Example of sharp tungsten tip electrochemically etched in NaOH solution.

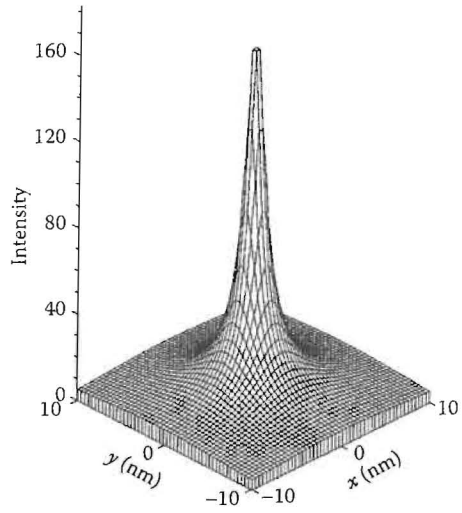

FIGURE 34.8 Calculated profile of plasmon resonance enhancement. (From Martin, O.J.F. and Girard, C., *Appl. Phys. Lett.*, 70, 705, 1997. With permission.)

In contrast to the shadowing effect, in some cases, such a well-sharpened metal tip strongly increases the effective light intensity beneath the STM tip. This is known as the field enhancement effect; the local electric field at the tunnel gap is increased by the plasmon resonance in the metallic tip, resulting from the physical shape of its nanometer-scale apex (Figure 34.8; Martin 1997). According to the literature, this effect can result in a light intensity magnification of as high as ×1000 under carefully prepared conditions. Since a light-induced STM signal is also enhanced, this effect is preferable for measurement. In addition, this also allows us to selectively excite a local area (~10 nm) of the sample, whose size is much smaller than the wavelength. Therefore, this effect increases the spatial resolution of light-induced STM.

34.2.5 Stray Light

The handling of stray light, as well as the stability of light source, is important for a photorelated measurement. A dark environment, for example, is the basis for the accurate measurement of STM-induced light emission (Section 34.4.6). In this respect, atomic force microscopy (AFM) that uses an optical system to measure the deflection of a lever is not suitable for a photorelated measurement. Some fraction of laser beams used inevitably illuminates the sample surface during observation and affects the measurement. Furthermore, the external illumination of the sample may affect the force detection of an optical lever. To solve these problems, a piezoresistive cantilever (Tortonese 1991), which can sense its deformation by itself without the aid of laser illumination, is used for a photorelated AFM measurement. Using a contact-mode AFM with a self-detecting cantilever, photocurrent mapping was performed over InAs nanowires grown at step edges on a GaAs substrate (Masuda 2005). In the experiment, the sample was intermittently illuminated with a variable-wavelength laser, and the nanoscale variation in photocurrent on the wires caused by the inhomogeneity of mechanical stress, composition, and defect density in the wires was observed.

34.3 Probing Carrier Dynamics in Semiconductors

This section describes the basic principles and techniques for probing carrier dynamics in nanoscale semiconductor structures.

34.3.1 Tip-Induced Band Bending and Surface Photovoltage

When STM is performed on a semiconductor sample, the (STM tip)–(tunneling gap)–(semiconductor sample) configuration forms an MIS structure, as shown in Figure 34.9. Here, a p-type semiconductor is used as a sample and a negative bias voltage is applied to the sample. In an STM/STS measurement performed under a dark condition at a certain bias voltage, tip-induced band bending (TIBB) appears owing to the leakage of the applied electric field into the sample, as illustrated in Figure 34.9a (Prins et al. 1996, Sommerhalter et al. 1997, Yoshida et al. 2006). When the sample below the STM tip is photoilluminated with a sufficient intensity, the redistribution of photoexcited carriers reduces band bending, resulting in the flat-band condition illustrated in Figure 34.9b. This change observed in the surface potential, change in the band bending, due to photoillumination is defined as SPV (Kronik and Shapira 1999). Since SPV is related to the local carrier dynamics induced by photoillumination, the analysis of SPV provides us information on the carrier dynamics in the sample.

When SPV is induced by photoexcitation, as shown in Figure 34.9, the barrier height (BH) for tunnel current decreases. Since the tunneling current is determined by the local density of states of the tip and sample and the transient probability that depends on BH, the reduction in BH due to SPV results in an increase in tunneling current. The difference in BH depends on the TIBB under the dark condition and is determined by the local carrier density. If a flat-band condition is achieved under the illuminated condition, the SPV spectrum represents TIBB. Therefore, by measuring the change in tunneling current due to photoillumination, we can observe the carrier density through the analysis of SPV.

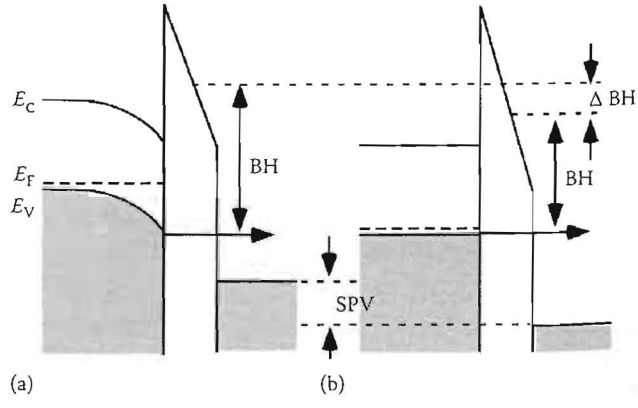

FIGURE 34.9 Schematic illustrations of metal–insulator–semiconductor (MIS) structures in cases (a) without and (b) with photoillumination (BH local barrier height).

Sections 34.3.2 and 34.3.3 show two laser-combined techniques that enable us to visualize the carrier dynamics in semiconductors on the nanoscale on the basis of the mechanisms of TIBB and SPV, namely, light-modulated scanning tunneling spectroscopy (LM-STS) and femtosecond time-resolved STM.

34.3.2 Light-Modulated Scanning Tunneling Spectroscopy

34.3.2.1 Basic Principle

A measurement technique in STM, STS, enables us to probe the local density of electronic states of materials on an atomic scale. In STS, the tunneling current versus sample bias voltage (I–V) curve is measured under a fixed tip-sample distance. The concept of LM-STS is to combine this technique with optical excitation. An I–V curve is measured under a chopped laser illumination (Figure 34.10a), which, for example, provides information on photocurrent generation and local carrier dynamics in a semiconductor sample (Takeuchi et al. 2004a,b).

Figure 34.10b and c shows an I–V curve obtained under a chopped laser illumination on a cleaved clean n-GaAs(110) surface and its magnification, respectively. The tunneling current oscillates at a chopping frequency of laser illumination, and two virtual I–V curves obtained from the envelopes, which correspond to those under dark (solid circles) and illuminated (open circles) conditions, can be simultaneously obtained. The SPV spectrum shown in Figure 34.10d is obtained by calculating the lateral shift of the two I–V curves with respect to the bias voltage for the I–V curve under the dark condition. For an n-type semiconductor, upward TIBB is induced under a positive sample bias voltage because no surface states exist within the band gap, and the tip can bend the bands until one of the band edges intersects with the Fermi level. In contrast, only a small downward band bending is induced at a negative sample bias voltage due to the Fermi-level pinning by the conduction band edge. If a flat-band condition is achieved under the illuminated condition, the SPV spectrum (Figure 34.10d) represents the bias voltage dependence of TIBB. Therefore, a large SPV is observed for a positive sample bias voltage. For the measurement on a p-type semiconductor, the opposite bias voltage dependence occurs.

34.3.2.2 Measurement on p–n Junction

As explained in Section 34.3.1, the magnitude of TIBB depends on the carrier density, and the minority-carrier dynamics in a semiconductor, which changes local carrier density, can be obtained with a nanoscale spatial resolution through the measurement of SPV by LT-STS (Yoshida et al. 2007).

The experimental setup of LM-STS measurement is illustrated in Figure 34.11. Here, a p–n junction was prepared by growing n-type (Si-doped, 2.0×10^{18} cm^{-3}, 500 nm) and p-type (Be-doped,

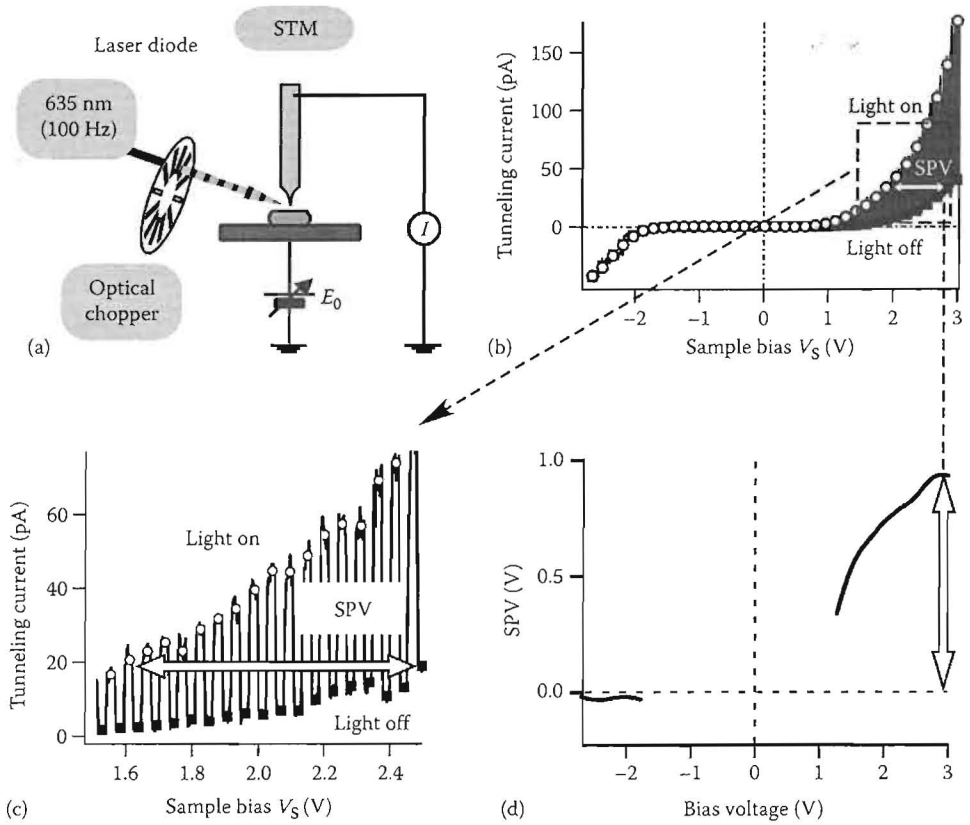

FIGURE 34.10 (a) Schematic illustration of experiment, (b) I–V curve obtained under chopped light, (c) magnification of I–V curve in (b), and (d) SPV (shift of I–V curves indicated by arrow in (b) plotted against bias voltage with respect to bias voltage for I–V curve under dark condition).

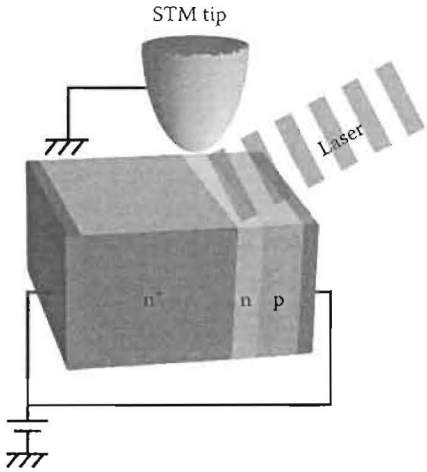

FIGURE 34.11 Schematic of LM-STS measurement setup.

2.0×10^{18} cm^{-3}, 500 nm) GaAs layers on an n-GaAs(001) substrate (Si-doped, 8.3×10^{18} cm^{-3}) using molecular beam epitaxy. Au–Zn Ohmic-contact electrodes were formed on both sides of the samples. LM-STS measurements were performed on a cleaved clean (110) surface at room temperature in ultrahigh vacuum ($<1 \times 10^{-8}$ Pa).

Spatially resolved LM-STS measurements were performed simultaneously with topographic imaging. The feedback loop of STM was opened at equally spaced measurement points during topographic imaging to fix the tip position, and an *I–V* curve was acquired under chopped light at each point. SPV was calculated from the *I–V* curves for the chosen bias voltages and presented with a gray scale.

Figure 34.12a shows the SPV images obtained at the p–n junction interface for positive (+2.5 V, up) and negative (−2.5 V, bottom) sample bias voltages. As described above, the magnitude of TIBB under a positive V_S is large (negligible) for the n-type (p-type) region, and the change in SPV across the p–n junction is thus clearly observed. In these images, a large SPV area at a positive (negative) V_S corresponds to the n-type region (p-type region).

When a forward bias voltage is applied to a p–n junction, minority holes (electrons) flow from the p-type (n-type) region to the n-type (p-type) region (Figure 34.12b), which decreases the magnitude of TIBB depending on the number of flowing minority carriers, as is explained in Section 34.3.1. Therefore, such dynamics of minority carriers can also be visualized by measuring SPV using LM-STS.

Figure 34.12c shows SPV images of a forward-biased p–n junction (V_F = 0.5–0.9 V). Since the decrease in SPV is related to the decrease in the magnitude of TIBB, the observed change is directly related to the change in the number of excess carriers below the STM tip. Using the logarithmic relationship of SPV with the minority-carrier density, the spatial distribution of minority carriers can be calculated from the SPV images (Figure 34.12d). The number of flowing minority carriers decreases with the distance from the p–n junction interface, owing to recombination with the majority carriers, as expected.

The inhomogeneous flow of minority carriers in a forward-biased p–n junction, shown in Figure 34.12, is considered to be

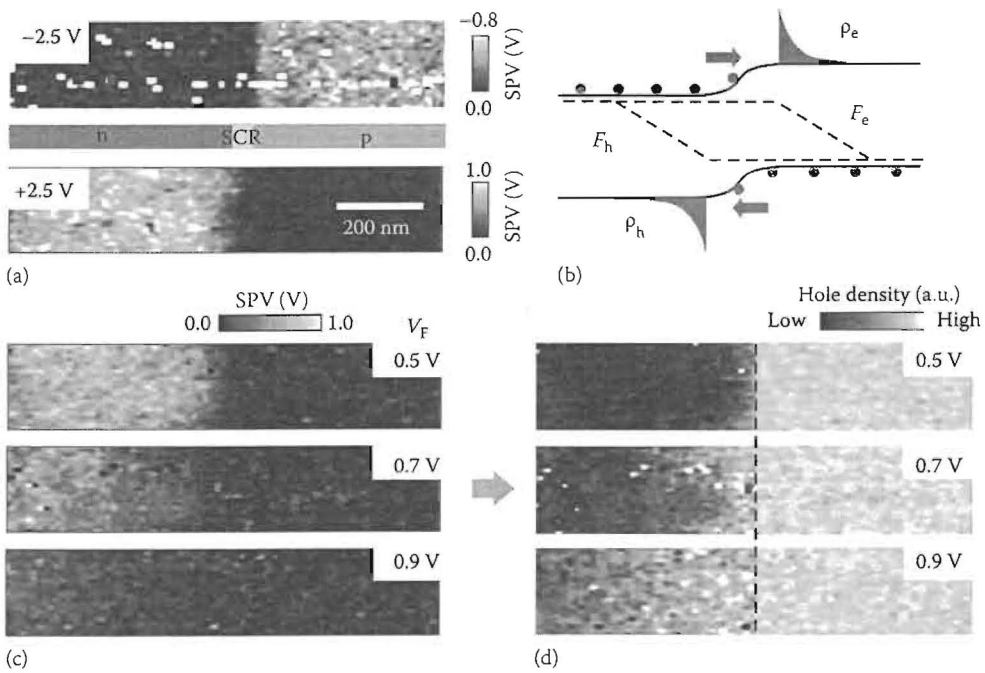

FIGURE 34.12 (a) SPV mappings of zero-bias (V_F = 0) p–n junction obtained at V_S = −2.5 V (*top*) and V_S = +2.5 V (*bottom*) (1000 × 200 nm, 80 × 20 LM-STS spectra). *SCR*: space charge region. (b) Band diagram of p–n junction with distribution of minority electrons (ρ_e) and holes (ρ_h) under forward-biased voltage condition. F_h and F_e denote the Fermi levels for holes and electrons, respectively. (c) SPV images of p–n junction with forward bias voltages. (d) Images of minority carrier (hole) flow calculated from (c).

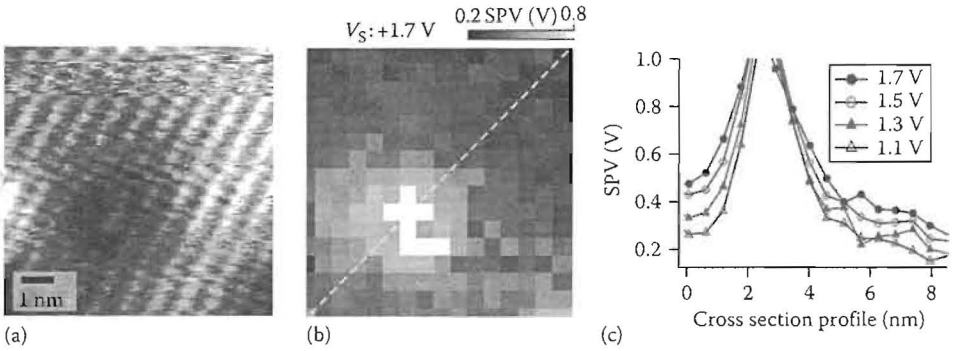

FIGURE 34.13 (a) Filled-state topographic image of Ga vacancy, (b) SPV image simultaneously obtained with topographic image in (a) (V_S = +1.7 V, 17 × 17 points), and (c) cross sections of SPV maps obtained at various bias voltages, along white line in (b).

caused by the nanoscale electrostatic potential fluctuation due to charged impurities, such as dopants and defects. The result indicates the importance of the method of evaluating the potential landscape on an atomic scale. In Section 34.3.2.3, a method of providing information on the modulation of the potential landscape around a single charged defect is presented (Yoshida et al. 2008).

34.3.2.3 Measurement on Charged Atomic Defect

Figure 34.13a shows a filled-state topographic image of a Ga vacancy on a GaAs (110) surface. The Ga vacancy exhibits a contrast of a bright elevation at the center of the defect location due to the dangling bond existing at the Ga vacancy that appears bright in a filled-state image. The surrounded dark area is caused by the depression region, originating from the screened Coulomb potential (SCP) around the negatively charged defect. Figure 34.13b shows the SPV image obtained for the same area in Figure 34.13a (V_S = +1.7 V). Since photoillumination reduces the magnitude of band bending around a charged defect with the same mechanism for reducing the magnitude of TIBB, the spatial variation in SPV represents the spatial variation in SCP. Figure 34.13c shows the cross-sectional profiles acquired at different bias voltages. Because of the effect of SCP, SPV, which has a maximum value at the center of the Ga vacancy, exponentially decreases with the distance from the center.

The magnitude of SPV increases with bias voltage; however, the spatial variation in cross-sectional profile remains unchanged. Since the shape of SCP is not affected by the bias voltage, the bias-dependent component of SPV originates from TIBB that shifts only the entire SPV profile along with bias voltage. Therefore, the spatial distribution of SPV directly represents SCP, and the charge state of the Ga vacancy can be determined by fitting the SPV profile with the SCP equation (McEllistrem et al. 1993).

34.3.3 Femtosecond Time-Resolved STM

34.3.3.1 History of Time-Resolved STM Development

"Smaller" and "faster" are the key factors in nanoscale science and technology. Indeed, important and interesting phenomena in various systems, such as the phenomena observed in functional materials and electronic devices, signal transfer in biosystems, and chemical reactions, are observed in the space range from several tens of nanometers to the single molecule and in the time range from several tens of picoseconds to the subpicosecond. However, it is extremely difficult to obtain spatial and temporal resolutions simultaneously on this scale. STM has an atomic-scale spatial resolution, but its temporal resolution is limited to less than 100 kHz owing to the circuit bandwidth, and the ultrafast carrier dynamics has been beyond the field of vision. In contrast, in leading-edge technology fields of quantum optics, wideband spectroscopy has been established, for example, using an ultrashort-pulse laser. However, the spatial resolution is generally limited to the wavelength. Therefore, since the invention of STM in 1982, combining ultrashort-pulsed-laser technology with STM has been one of the most attractive targets (Hamers and Markert 1990, Grafström 2002, Shigekawa et al. 2005, 2008, Yamashita et al. 2005).

An optical pump-probe technique is a prominent method, in which a sample is illuminated with a sequence of paired laser pulses with a certain delay time t_d. A pump pulse with a high peak intensity excites the sample, and a subsequently arriving probe pulse with a low peak intensity tracks the temporal evolution of the excited stated induced by the first pump pulse (Othonos 1998, Shah 1999). For example, in optical pump-probe reflectivity (OPPR) measurement (Figure 34.14a), the reflectivity of the probe pulse R is measured as a function of delay time t_d between two pulses, which is often performed by recording the reflected light intensity using a photodiode. When the pump-probe pair repeatedly illuminates the surface at a repetition of 1 k–100 MHz, the photodiode detector does not need to resolve each temporal profile of the reflected light intensity, but it only needs to detect the time-averaged intensity. The dependence of reflectivity R on delay time gives a measure of the relaxation of the excited states induced by a pump. The temporal resolution attainable in such experiments is limited only by the pulse width, which is generally in the femtosecond range.

If the tunneling caused by optical excitation can be measured by STM, high temporal and spatial sensitivities can be simultaneously achieved with the atomic-scale resolution of STM (Shigekawa et al. 2005, 2008). A pulse-pair-excited STM (PPX-STM)

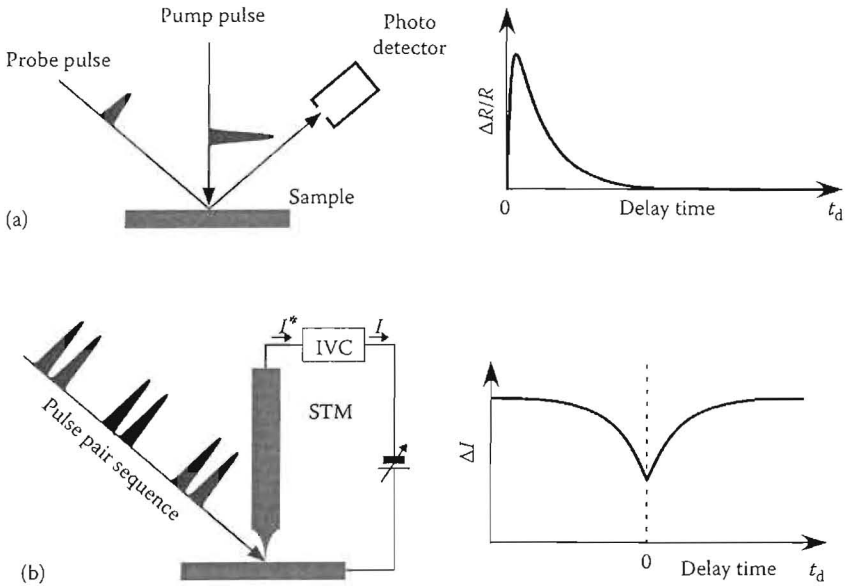

FIGURE 34.14 Principle of (a) OPPR and (b) PPX-STM measurements.

system has been a promising setup, in which, in analogy with pump-probe experiments, a sequence of paired laser pulses with a certain delay time t_d illuminates a sample surface beneath the STM tip, and the tunneling current I is measured as a function of t_d (Figure 34.14b). However, efforts toward its realization failed because of experimental difficulties. In most cases, the delay-dependent current component is so faint (~10^{-3} of the average current) that lock-in detection with a modulation technique is required for observation. In purely optical pump-probe experiments, the laser intensity is generally modulated; however, this technique is not directly applicable to PPX-STM because it induces the thermal expansion and shrinking of the STM tip in synchronization with modulation, and consequently results in a large change in tunneling current. To suppress this thermal effect, retracting the STM tip far away from the surface has been attempted by many researchers; however, in this case, the detected signal was not a tunneling current but a displacement current or photoelectron current, and thus, no spatial resolution higher than 1 μm has been attained (Hamers and Markert 1990).

34.3.3.2 Shaken-Pulse-Pair-Excited STM

A more applicable technique is shaken-pulse-pair-excited STM (SPPX-STM) (Takeuchi et al. 2004a,b, Terada et al. 2007), which has been developed using the principle of PPX-STM. As described above, in PPX-STM, in analogy with the pump-probe technique, a sequence of paired laser pulses with a certain delay time t_d illuminates a sample surface beneath the STM tip, and the tunneling current I is measured as a function of t_d (Figure 34.14b). When the paired optical pulses arrive at the sample, they generate current pulses in the raw tunneling current I^*, reflecting the excitation and relaxation of the sample (Figure 34.15a). If these current pulses decay faster than the time scale of the STM preamplifier bandwidth, they are temporally averaged in the preamplifier and cannot be detected directly in the signal I. Even in this case, the relaxation

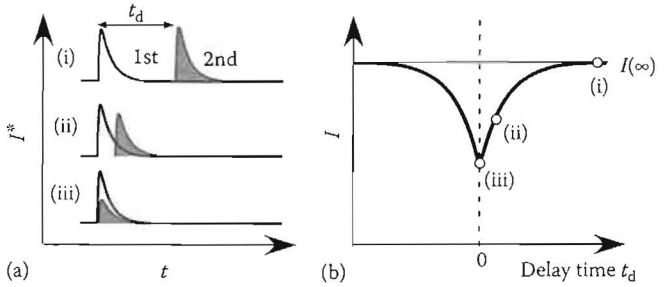

FIGURE 34.15 (a) Relationship between raw tunneling current I^* and delay time t_d. (b) Measured tunneling current I as function of delay time, where delay times of (i), (ii), and (iii) correspond to those of (i), (ii), and (iii) in (a).

dynamics can be probed through the t_d dependence of I, as shown in Figure 34.15.

When t_d is small, that is, the second probe arrives at the sample excited by the first pump and not relaxed, the second tunneling-current pulse changes under the strong effect of excited states (Figure 34.15-iii), as opposed to the case in which the probe arrives when the states excited by the pump are completely relaxed (Figure 34.15-i). As t_d increases, the effect of the pump becomes smaller (Figure 34.15-ii), and eventually, at a large t_d, the tunneling current I saturates to a value $I(\infty)$ (Figure 34.15-i). Then, $\Delta I(t_d) \equiv I(t_d) - I(\infty)$ provides information on excited states at the delay time t_d after pump excitation. This technique has a temporal resolution of pulse width equivalent to that of ultrafast spectroscopy (a few femtoseconds) and a spatial resolution of tunneling current equivalent to that of STM (subangstrom).

In SPPX-STM, the delay time is modulated instead of the laser intensity for lock-in detection. To date, two optical setups have been used for delay time control. One is a mechanically controlled setup, which is used in conventional interferometers.

In this setup, a corner-cube mirror is inserted into a pump or probe optical line and is mechanically shaken to periodically modulate the optical lengths. The other is an electro-optically controlled setup, in which the polarization plane of a part of a pulse sequence is electrically rotated with an electro-optic modulator, so that pulses are "picked" by a polarizing beam splitter to generate a desired pulse sequence. The delay time is periodically modulated by changing the timing of picking pulses from the pump and probe pulse sequences. The latter method is superior to the former in performance characteristics, such as the wide delay time range (up to a few microseconds), the high signal-to-noise ratio, the high signal level, and the stability of the optical line, and therefore, it is more suitable for SPPX-STM measurement.

34.3.3.3 Basic Principle of SPPX-STM Measurement on Semiconductors

Although the basic principle of PPX-STM is simple, the underlying physics is not straightforward. Here, an SPPX-STM measurement is assumed to be performed under the condition in which an MIS diode formed by a sample and a tip is reversely biased. As in the case of LM-STS measurements, TIBB occurs in the surface region in the dark owing to the leakage of the electric field into the sample (Figure 34.16a). With optical illumination (Figure 34.16b), the charge separation of photocarriers occurs owing to the electric field, where majority carriers flow into the bulk side and minority carriers are trapped at the surface. This carrier redistribution reduces the electric field and changes the surface potential, which is called SPV (Section 34.3.1), and increases the effective bias voltage applied to the tunnel junction (Figure 34.16c). Consequently, the illumination increases the raw tunneling current I^*.

The excited state subsequently relaxes to the original state through two processes. One is the decay of the photocarriers on the bulk side (bulk-side decay) via recombination, drift, and diffusion (Figure 34.16d). The other is the decay of the carriers trapped at the surface (surface-side decay) via thermionic emission and recombination with counterpart carriers tunneling from the tip (Figure 34.16e). When the tunneling current is low, few counterpart carriers exist near the surface, and hence, the surface-side decay constant is longer than the bulk-side decay constant. Both of these decay processes appear in the SPPX-STM signal as follows.

The bulk-side decay is probed through the mechanism of absorption bleaching, which also provides a basis of OPPR measurement in some cases. If the bulk-side carriers remain when the second optical pulse arrives, the absorption of the second optical pulse is suppressed, which depends on the bulk-side carrier density at the moment. The corresponding decrease in I^* is detected through the decrease in I; hence, $\Delta I(t_d)$ is a measure of the bulk-side carrier density at the delay time t_d after the excitation by the first optical pulse. On the other hand, the surface-side decay is probed through the mechanism related to the charge-separation efficiency instead of photocarrier generation. If the surface carriers remain when the second optical pulse arrives, the electric field in the surface region remains low. Therefore, the excited photocarriers are less efficiently trapped at the surface. Thus, the SPV generated by the second optical pulse decreases, and the height of the second current pulse in I^* also decreases. Accordingly, $\Delta I(t_d)$ is a measure of the surface-side carrier density at the delay time t_d as well as the bulk-side carrier density. The decay constants for both components are derived from the fitting of $\Delta I(t_d)$ by a double exponential function; the

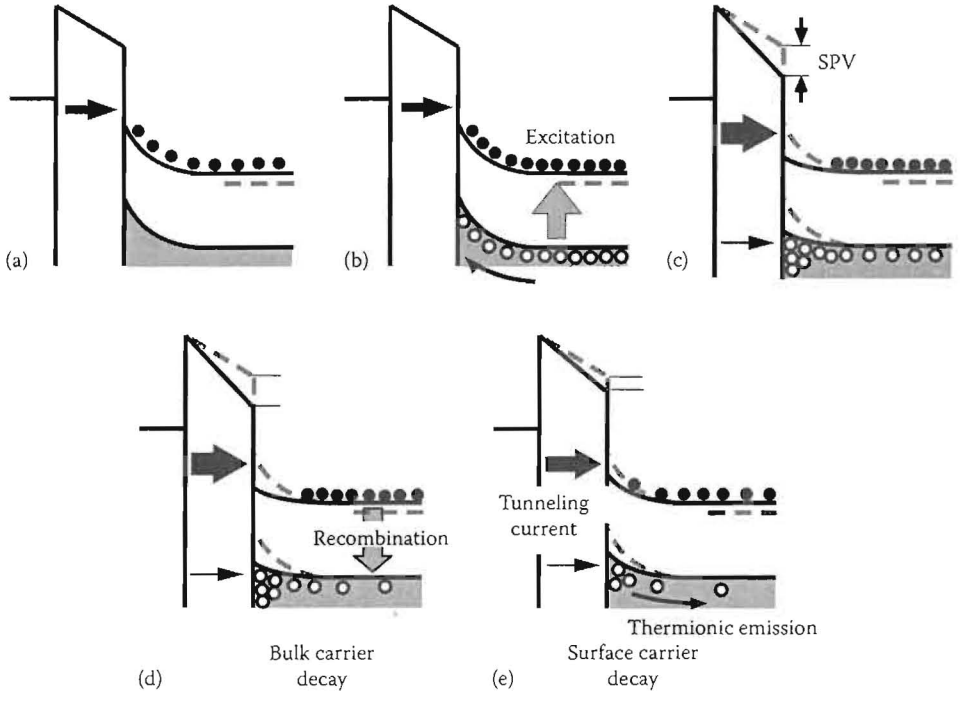

FIGURE 34.16 Time evolution of band diagram for n-type semiconductor due to laser pulse excitation under reversely biased condition: (a) in dark, (b) arrival of laser pulse, (c) after redistribution of excited carriers, (d) bulk-side carrier decay, and (e) surface-side carrier decay.

shorter time constant τ_b is attributed to the bulk-side decay, and the longer time constant τ_b to the surface-side decay.

34.3.3.4 Carrier Dynamics Probed by SPPX-STM

As an example of SPPX-STM measurement results, carrier decay spectra via recombination in bulk (τ_b component) for a $GaN_{0.36}As_{0.64}$ sample are shown in Figure 34.17. The same sample was measured by both SPPX-STM (Figure 34.17a) and OPPR (Figure 34.17b), using a pulse laser with a wavelength of 800 nm, a pulse width of 120 fs, and a repetition frequency of 90 MHz. The time-resolved signal $\Delta I(t_d)$ has a minimum value when $t_d = 0$ and exponentially decays toward zero as t_d increases. The negative sign of the $\Delta I(t_d)$ signal, which corresponds to the decrease in I, agrees with an absorption bleaching mechanism. The decay constant was obtained from the exponential fitting of $\Delta I(t_d)$ to be 444 ps, in good agreement with the bulk-recombination lifetime determined by the temporal evolution of the reflectivity change $\Delta R/R$ (406 ps).

Another example of SPPX measurement results is shown by two-dimensional (2D) maps of SPPX-STM signals obtained for a low-temperature-grown GaAs (LT-GaAs)/$Al_{0.5}Ga_{0.5}As$/GaAs sample. LT-GaAs contains high-density defects that act as recombination sites for carriers. Thus, its carrier lifetime is much shorter than that of GaAs. The AlGaAs barrier layer has a band gap larger than the optical excitation. As expected, the LT-GaAs region exhibits an ultrafast decay component with a time constant of 4 ps, whereas the GaAs region exhibits a time constant of 4.8 ns. These values are consistent with the recombination lifetimes determined by OPPR measurement, namely, 1.5 ps and 2.7 ns for the LT-GaAs and GaAs samples, respectively.

For the spatial mapping of $\Delta I(t_d)$, two modes are possible. One is a constant delay-time mode, where the values of $\Delta I(t_d)$ are recorded for each t_d while the STM tip is scanning the surface. The other is a grid mode. In this mode, the scan area is divided by scan grid points, similarly to that in the case of STS. During the STM scan, the tip is fixed at each grid point and $\Delta I(t_d)$ is measured as a function of t_d.

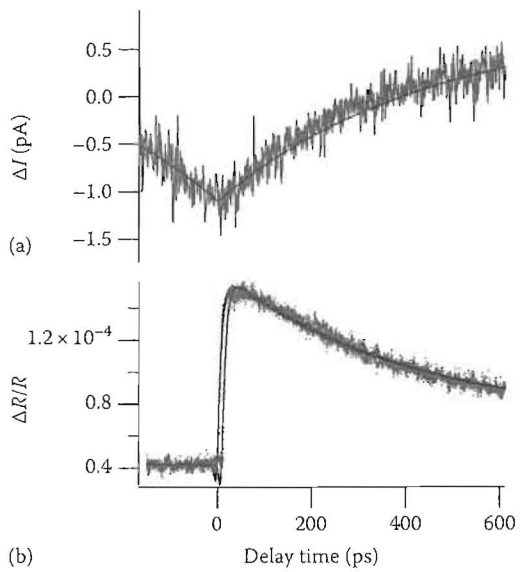

FIGURE 34.17 Carrier decay spectra via recombination in bulk (τ_b component) for $GaN_{0.36}As_{0.64}$ sample measured by (a) SPPX-STM and (b) OPPR.

Figure 34.18 shows $\Delta I(t_d)$ maps for t_d = 2, 31 ps, 11, and 200 ns obtained using the constant delay-time mode, together with the STM topographic image (top). At 2 ps, a clear contrast is observed across the AlGaAs/LT-GaAs boundary, which becomes smaller as t_d increases. As the magnitude of $\Delta I(t_d)$ corresponds to that of absorption bleaching, Figure 34.18 shows the spatial distribution of photoexcited carrier density at each t_d after excitation. In this manner, $\Delta I(t_d)$ maps for different t_d values provide spatial information on carrier density at different times. Combining the STM topography with the atomic-scale spatial resolution makes it possible to investigate the fundamental processes of the carrier dynamics.

By combining an advanced ultrashort-pulsed-laser technology with STM, a new microscopy technique is realized that enables the probing and direct analysis of the various carrier dynamics modulated in a nanometer-scale potential landscape (Terada et al. 2010).

34.4 Other Techniques

This section introduces some other cases.

34.4.1 With Optical Manipulation

The simplest photorelated technique is a comparison of STM/AFM images obtained before and during, or after illumination. Figure 34.19 shows an example of such a technique: a derivatized azobenzene molecule, a typical photoactive isomer, adsorbed on a gold substrate was alternately illuminated by visible and ultraviolet lights, and the corresponding change in molecular shape was observed by STM, showing the change in intramolecular electronic structure due to photoisomerization (Yasuda et al. 2003). The structural change in molecules due to photoexcitation is also detectable using AFM by measuring the force induced by the change in the length of molecules bridged between the tip and the substrate (Hugel et al. 2002).

Figure 34.20 shows another example, that is, the desorption of adatoms on a Si(111)-7 × 7 surface using ultrashort-pulsed-laser irradiation (Futaba et al. 2003). It was shown that one of the four types of adatoms could selectively be desorbed by tuning the temporal separation of successive pulse excitations to the molecular vibration periodicity of the target adatom.

The metal–insulator transition (MIT) of low-dimensional materials is one of the most attractive phenomena observed in the research studies of phase transitions. One-dimensional (1D) nanowires are nanoscale building blocks that can efficiently transport electrical charges that constitute information on nanoelectronics, and an In/Si nanowire system, for example, has

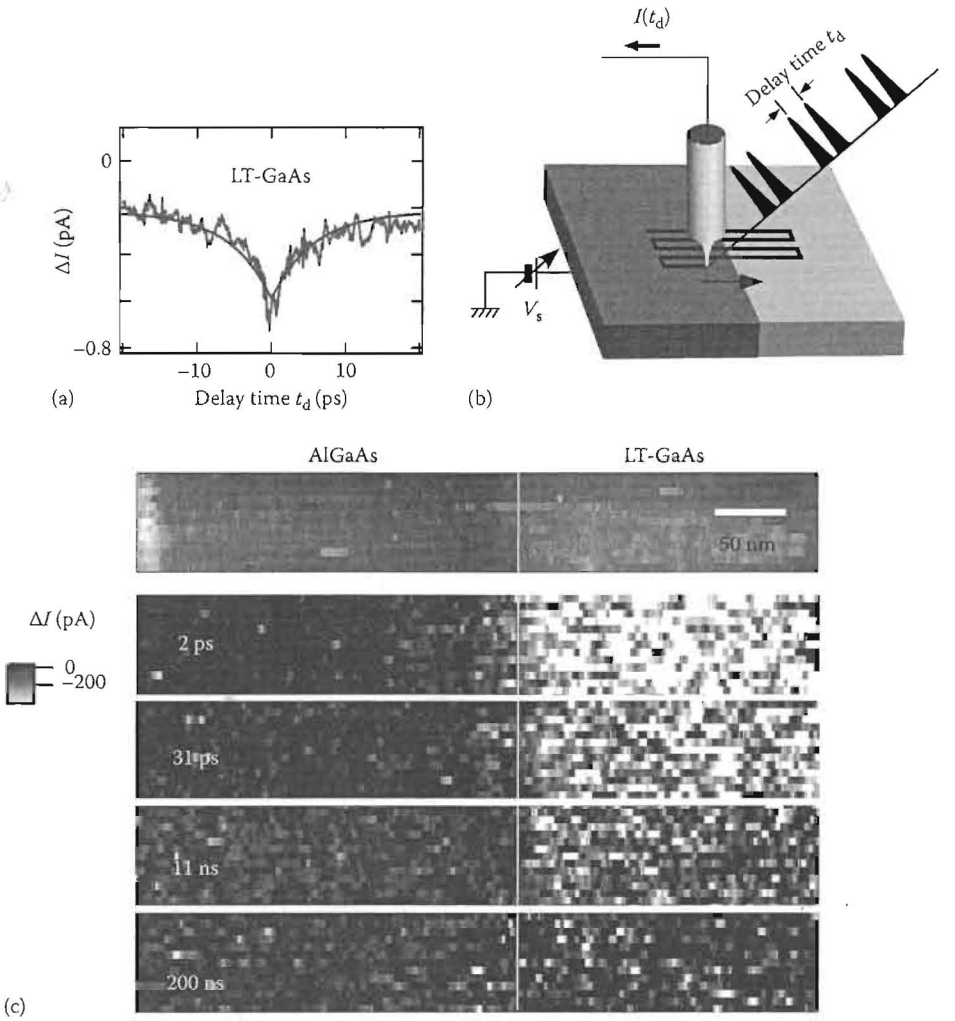

FIGURE 34.18 Two-dimensional maps of SPPX signal obtained for LT-GaAs/$Al_{0.5}Ga_{0.5}As$/GaAs sample. (a) Carrier decay via recombination in bulk for LT-GaAs region. (b) Schematic of constant delay-time mode. (c) Two-dimensional maps of SPPX signal obtained for sequential delay times.

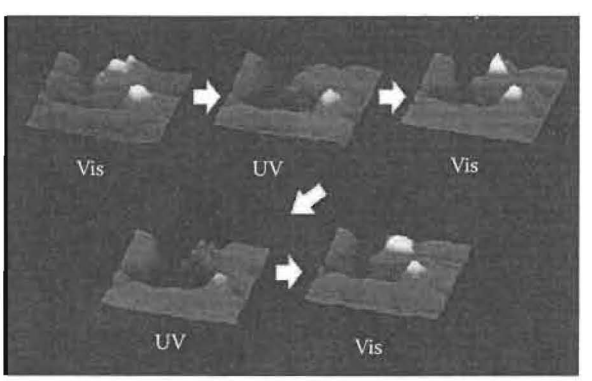

FIGURE 34.19 STM observation of photoactivated isomerization of azobenzen derivative molecule.

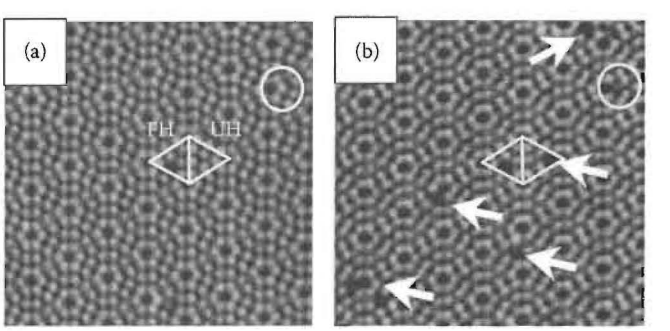

FIGURE 34.20 Si(111) clean surface (a) before and (b) after adatom desorption due to femtosecond pulsed-laser irradiation. (From Futaba, D. N. et al., *Appl. Phys. Lett.*, 83, 2333, 2003. With permission.)

extensively been studied. This system has a metal/semiconductor structure, and surface band bending, caused by charge transfer at the interface, was found to prevent MIT even below the critical temperature owing to the shift in Fermi level from the half-filled state (Terada et al. 2008). Using laser-combined STM, a reversible MIT due to the band filling of the 1D surface state by the optical doping of carriers was observed (Figure 34.21).

These examples indicate that the laser-combined STM provides useful information on the nanoscale by observing the structural and electronic changes manipulated by photoexcitation.

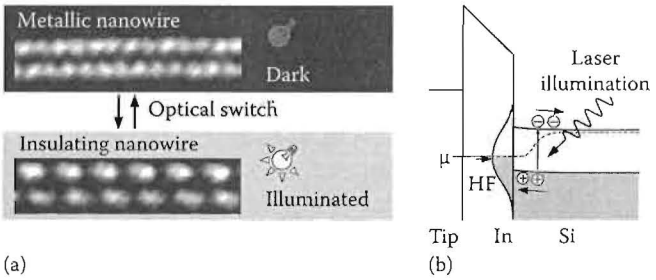

FIGURE 34.21 Schematic illustrations of metal–insulator transition of In/Si nanowire by optical doping (a) and band-filling mechanism (b). SPV reduces TIBB (Section 34.3.1), resulting in the change in the magnitude of band filling.

34.4.2 Optical Modulation of Bias Voltage

When STM is combined with photoillumination, a photoinduced change in tunnel current, other than the structural changes represented in Section 34.4.3, reflects various important sample properties when a suitable measurement condition is adopted (Grafström 2002). When a sample is illuminated with a p-polarization geometry, the oscillating electric field of the light induces a small high-frequency modulation of the bias voltage at the tunnel gap. This ac modulation in turn induces a small change in dc current when the I–V characteristics of the tunnel junction are nonlinear, as explained below. If the bias voltage is modulated as $V_0 + \Delta V \sin \omega t$, the tunnel current responds to it as $I(V_0 + \Delta V \sin \omega t)$. Then, its dc component can be approximated as $I(V_0) + (\partial^2 I/\partial V^2)\Delta V^2/2$ (Bragas 1997). Thus, the photoinduced current becomes proportional to $\partial^2 I/\partial V^2$ and the square of the modulation amplitude. With this concept, the ultrafast propagation of voltage pulses along a gold transmission line was detected by pulse-laser-combined time-resolved STM with a time resolution of 10 ps (Khusnatdinov et al. 2000). Although the origin of the spatially resolved contrast was the variation in dI/dV characteristics rather than the transient phenomenon itself, a spatial resolution of 1 nm was achieved with the temporal resolution.

34.4.3 With Variation in Photoexcitation Wavelength

In this method, tunnel current or displacement current is measured as a function of photoexcitation wavelength. With the modulation of the electric field applied to a sample, interband transition energies in semiconductors is analyzed on the nanoscale by detecting the change in the generation of the STM current reflecting the change in optical absorption coefficient depending on the wavelength (Hida et al. 2001). The chopping frequency should be chosen high enough to remove the thermal expansion effect (Section 34.2.1). An advanced rapid acquisition of reliable photoabsorption spectra has been realized by Fourier transform (FT) photoabsorption spectroscopy (Naruse et al. 2007), in which samples are illuminated with a multiplexed light from an FT interferometer, and the corresponding change in tunneling current is measured using an interferogram to obtain an FT spectrum.

34.4.4 Spin-Polarized Excitation

STM observation with an optically pumped GaAs tip allows us to conduct spin-sensitive STM measurements (Suzuki 1997). When the tip is illuminated by a circularly polarized laser, a spin-polarized population of electrons in the conduction band is produced. This is due to the spin-orbit splitting of the p-like valence band and the selection rules for optical transitions (Pierce and Meier 1976). The tunnel current from such a tip is sensitive to the magnetization of the sample surface. Magnetic domains of several hundred nanometer size in a Co thin film were imaged using this technique.

34.4.5 With Synchrotron Radiation

The combination of STM with synchrotron radiation has been studied to realize atom-resolved elemental identification (Saito et al. 2006), in which sample was intermittently illuminated by a mechanically chopped hard x-ray (~11 keV) from a synchrotron under a total reflection condition. The photoinduced current was detected by a lock-in amplifier and spatially mapped simultaneously with the STM topography, as shown in Figure 34.22. While no contrast in photoinduced current was obtained for x-rays with energies below the absorption edge of the inner core electron of a Ge atom, a clear contrast appeared with a spatial variation of a few nanometers when the energy was above the absorption edge, as shown in Figure 34.22b. Although the physical origin of the photoinduced current is not fully understood yet, this technique has the potential of realizing x-ray absorption spectroscopy on a single atom. To obtain a high resolution, a coating STM tip has been considered to block photoinduced electrons impinging on the sidewall of the tip and extract photoelectron current from a small area below the tip apex (Akiyama et al. 2005, Eguchi et al. 2006).

34.4.6 STM-Induced Light Emission

STM luminescence spectroscopy, which is also called photon STM measurement, is used to investigate local photoluminescence properties of conductive samples. It measures the inverse

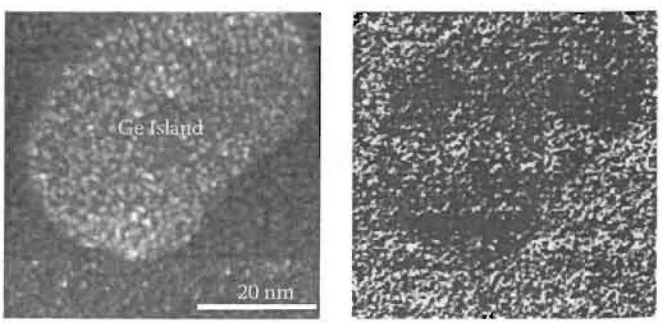

FIGURE 34.22 Ge island on Si(111) substrate observed by synchrotron-radiation-based STM. (a) STM topography and (b) photoinduced current by x-ray with energy above Ga adsorption edge. (From Saito, A. et al., *J. Synchrotron Rad.* 13, 216, 2006. With permission.)

photoelectric effect stimulated by the electrons or holes injected from an STM tip to the sample during STM measurement. The injected carriers cause photon emission via various physical phenomena that depend on the sample material, namely, surface plasmon polariton excitation in metallic samples, LUMO-HOMO transition in molecular samples (Qiu 2003), and interband transition in semiconductor samples (Sakurai 2004). The emitted photons are collected using lenses or concave mirrors into an optical fiber and guided to a spectrometer. Under a moderate condition, photon intensities up to 1000 count per second (cps) can be obtained.

Figure 34.23 shows STM luminescence spectra from a ZnEtioI molecule adsorbed on a thin alumina film grown on an NiAl substrate. The intramolecular position of the tunnel current injection was precisely selected on one of the four submolecular lobes, as shown in the inset. After a suitable normalization, the three spectra measured using three different STM tips were observed to be identical, showing the fluorescence spectrum due to the LUMO-HOMO transition of electrons, with equally spaced (spacing: 40 ± 2 meV) small peaks marked by vertical lines in Figure 34.23a. These peaks correspond to molecular vibration excitations in the fluorescence process, as also observed in macroscopic fluorescence spectroscopy. These results suggest that STM luminescence realizes the vibrational spectroscopy of molecules with a submolecular resolution.

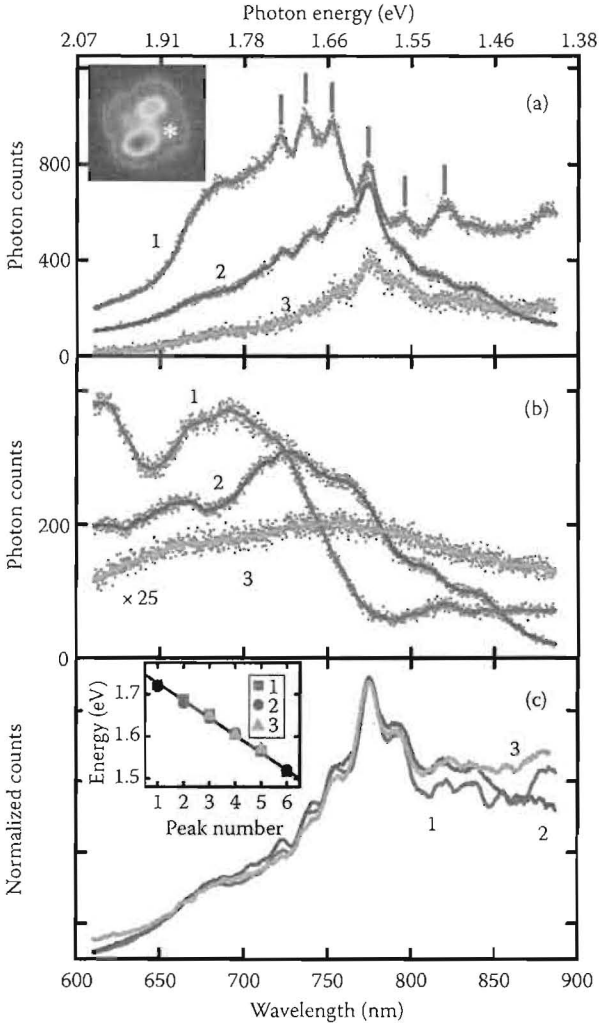

FIGURE 34.23 Vibrationally resolved fluorescence from one of the four submolecular lobes of ZnEtioI molecule (inset). (a) Raw fluorescence spectra from molecule with three different STM tips: Ag tips for spectra 1 and 2 and W tip for spectrum 3. (b) Raw spectra from NiAl substrate with same tips. (c) Smoothed molecular spectra (a) were divided by substrate spectra (b) for normalization. (From Qiu, X. H. et al., *Science*, 299, 542, 2003. With permission.)

34.4.7 With Near-Field Optics

Near-field scanning optical microscopy (NSOM), a SPM that uses light as a probe, was developed in 1984 (Pohl 1984, Kim and Song 2007). A typical setup is illustrated in Figure 34.24. A sample surface is scanned using an optical fiber with a small aperture to investigate the local optical properties of the sample. The fiber is used either for illuminating the local area of the sample or for collecting photons from the sample, or for both of them. Far-field optical access to the sample may also be adopted, using a conventional optical microscope or a simple lens. The high spatial resolution of NSOM is based on the geometrical setup, where a subwavelength-scale light source or light detector (the small aperture in Figure 34.24) is placed at a subwavelength distance from the sample. Under such conditions, the electromagnetic field around the probe contains a large fraction of nonpropagating, evanescent (near-field) waves that decay exponentially as a function of the distance from the probe. Consequently, the area sensitively probed is determined by the probe size (aperture size), not by the light wavelength. The NSOM probe with a small aperture is made, for example, by pulling a heated optical fiber until it is elongated, thinned, and eventually broken. Successive chemical etching and

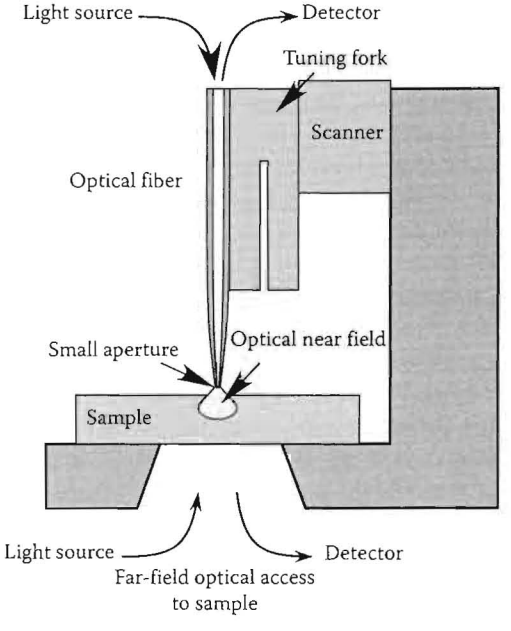

FIGURE 34.24 Typical NSOM setup.

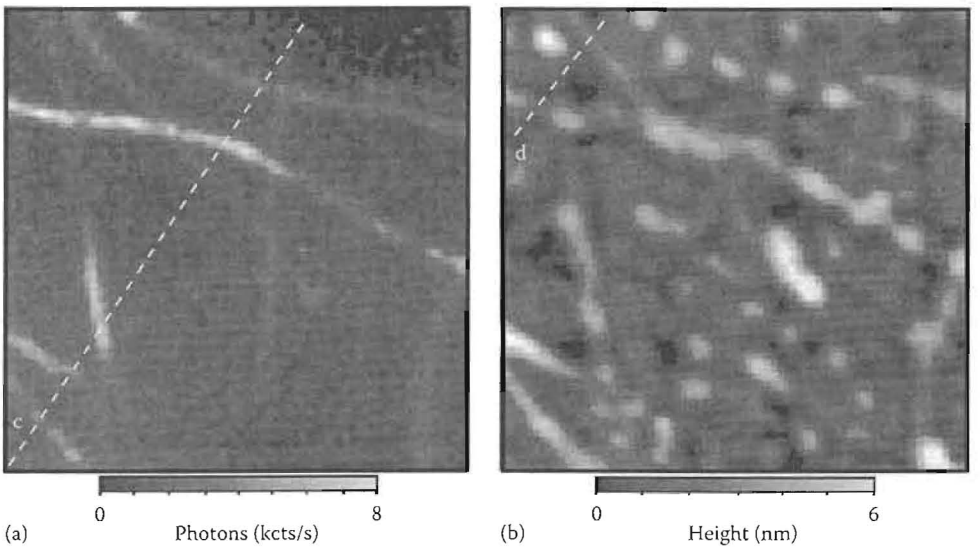

FIGURE 34.25 AFM-enhanced Raman microscopy of single-walled carbon nanotubes. (a) Raman intensity mapping and (b) AFM topography of same area. The scan area is $1 \times 1\,\mu m^2$. (From Hartschuh, A. et al., *Phys. Rev. Lett.*, 90, 095503, 2003. With permission.)

metal coating are also carried out to reduce the aperture diameter and to maximize the throughput of the aperture, respectively. The resolution achieved by such an aperture is ~30 nm. On the other hand, an apertureless NSOM has a higher resolution, ~10 nm (Kawata and Inouye 1995, Kawata et al. 1999, Novotny et al. 1995). An example is STM-enhanced Raman spectroscopy (Hartschuh et al. 2003), where the intensity of the far-field illumination with a spot size of a few micrometers is locally increased by the field enhancement effect by the AFM sharp metal tip. Figure 34.25 shows the high-resolution near-field Raman microscopy of single-walled carbon nanotubes conducted with AFM-enhanced Raman microscopy (Hartschuh et al. 2003).

To achieve a high spatial resolution, the regulation of the probe-sample distance at a certain subwavelength value (typically 1–50 nm) is important. When both the sample and the probe are conductive, an STM regulation mode, where the tunnel current between the probe and the sample is used to measure the distance, can be employed. For nonconductive samples, the distance is often controlled by an AFM regulation mode. For example, as shown in Figure 34.19, the optical fiber is mounted on a quartz tuning fork and oscillated parallel to the sample surface by a self-oscillator circuit. When the probe apex approaches the sample surface, the resonant frequency of the tuning fork shifts slightly, which gives the measure of the probe-sample distance.

Time-resolved NSOM is also a promising method for observing the carrier dynamics in materials and has been developed to provide the spatial and temporal resolutions of ~150 nm and ~150 fs, respectively (Levy et al. 1996, Nechay et al. 1999, Nagahara et al. 2004).

34.4.8 Fabrication

Laser-combined STM and related techniques can be used not only for the investigation of material properties but also for the fabrication of nanostructures (Jersch and Dickmann 1996, Lu 2000, Chimmalgi et al. 2005, Wang 2005). As described in Section 34.2, photo-irradiation on nanoprobes of STM and AFM, for example, causes the thermal expansion of the nanoprobes. Therefore, when probe position and pulsed-laser irradiation are designed, the mechanical indentation of sample surface is performed in a controlled manner. On the other hand, the field enhancement effect induced by p-polarized laser illumination is known to generate extremely localized stress accumulation in the subwavelength area beneath the nanoprobes, which mechanism is applicable for fabrication. This method is superior to the mechanical indentation because of the less damage on the probe apex. A demonstrative study shows that nanotrenches as narrow as 10 nm can be reproductively fabricated on an Au thin film with such a technique (Chimmalgi et al. 2005).

34.5 Summary

In this chapter, new microscopy techniques realized by combining STM and related techniques with optical technologies have been described in detail. The methods with high potentials that, for example, enable the investigation and real-space imaging of nanoscale electronic and structural dynamics induced by optical excitation have been explained. The direct view of such dynamics enables further advancement in nanoscale science and technology. Although it is difficult to cover all related topics, the materials discussed in this chapter are presented in a form that is instructive to nonspecialists as well as specialists. Understanding the basic mechanisms of the new microscopy techniques makes it possible to develop the ability of handling the issues we face in the measurement using the new microscopy techniques. With ingenuity, a new method can be developed.

References

Akiyama, K., Eguchi, T., An, T., and Hasegawa, Y. 2005. Fabrication of a glass-coated metal tip for synchrotron-radiation-light-irradiated scanning tunneling microscopy. *Rev. Sci. Instrum.* 78, 8: 083711.

Bragas, A.V. 1997. Spectroscopic response of photoinduced currents in a laser-assisted scanning tunneling microscope. *J. Appl. Phys.* 82: 4153–4158.

Chimmalgi, A., Grigoropoulos, C.P., and Komvopoulos, K. 2005. Surface nanostructuring by nano-/femtosecond laser-assisted scanning force microscopy. *J. Appl. Phys.* 97: 104319-1–104319-12.

Eguchi, T., Okuda, T., Matsushima, T., Kataoka, A., Harasawa, A., Akiyama, K., Kinoshita, T. et al. 2006. Element specific imaging by scanning tunneling microscopy combined with synchrotron radiation light. *Appl. Phys. Lett.* 89:243119.

Futaba, D.N., Morita, R., Yamashita, M., Tomiyama, S., and Shigekawa, H. 2003. Site-selective silicon adatom desorption using femtosecond laser pulse pairs and scanning tunneling microscopy. *Appl. Phys. Lett.* 83: 2333–2335.

Grafström, S. 1998. Thermal expansion of scanning tunneling microscopy tips under laser illumination. *J. Appl. Phys.* 83: 3453–3460.

Grafström, S. 2002. Photoassisted scanning tunneling microscopy. *Appl. Phys. Rev.* 91: 1717–1753.

Hamers, R.J. and Cahill, G.D. 1991. Ultrafast time resolution in scanned probe microscopies: Surface photovoltage on Si(111)-7x7. *J. Vac. Sci. Technol.* B9: 514–518.

Hamers, R.J. and Markert, K. 1990. Atomically resolved carrier recombination at Si(111)-7×7 surfaces. *Phys. Rev. Lett.* 64: 1051–1054.

Hartschuh, A., Sánchez, E.J., Xie, X.S., and Novotny, L. 2003. High-resolution near-field Raman microscopy of single-walled carbon nanotubes. *Phys. Rev. Lett.* 90: 095503-1–095503-4.

Hida, A., Mera, Y., and Maeda, K. 2001. Electric field modulation spectroscopy by scanning tunneling microscopy with a nanometer-scale resolution. *Appl. Phys. Lett.* 78: 3029–3031.

Hugel, T., Holland, N.B., Cattani, A., Moroder, L., Seitz, M., and Gaub, H.E. 2002. Single-molecule optomechanical cycle. *Science* 296: 1103–1106.

Jersch, J. 1999. Time-resolved current response of a nanosecond laser pulse illuminated STM tip. *Appl. Phys. A* 68: 637–641.

Jersch, J. and Dickmann, K. 1996. Nanostructure fabrication using laser field enhancement in the near field of a scanning tunneling microscope tip. *Appl. Phys. Lett.* 68: 868–870.

Kawata, S. and Inouye, Y. 1995. Scanning probe optical microscopy using a metallic probe tip. *Ultramicroscopy* 57: 313–317.

Kawata, Y., Xu, C., and Denk, W. 1999. Feasibility of molecular-resolution fluorescence near-field microscopy using multi-photon absorption and field enhancement near a sharp tip. *J. Appl. Phys.* 85: 1294–1301.

Khusnatdinov, N.N., Nagle, T.J., and Nunes, G. 2000. Ultrafast scanning tunneling microscopy with 1 nm resolution. *Appl. Phys. Lett.* 77: 4434–4436.

Kim, J.H. and Song, K.B. 2007. Recent progress of nano-technology with NSOM. *Micron* 38: 409–426.

Kronik, L. and Shapira, Y. 1999. Surface photovoltage phenomena: Theory, experiment, and applications. *Surf. Sci. Rep.* 37: 1–206

Levy, J., Nikitin, V., Kikkawa, J.M., Cohen, A., Samarth, N., Garcia, R., and Awschalom, D.D., 1996. Spatiotemporal near-field spin microscopy in patterned magnetic heterostructures. *Phys. Rev. Lett.* 76: 1948–1951.

Lewis, A. 1984 Development of a 500 Å spatial resolution light microscope. *Ultramicroscopy* 13: 227–231.

Lu, Y.F., Mai, Z.H., Zheng, Y.W., and Song W.D. 2000. Nanostructure fabrication using pulsed lasers in combination with a scanning tunneling microscope: Mechanism investigation. *Appl. Phys. Lett.* 76: 1200–1202.

Martin, O.J.F. and Girard, C. 1997. Controlling and tuning strong optical field gradients at a local probe microscope tip apex. *Appl. Phys. Lett.* 70: 705–707.

Masuda, H. 2005. Local photocurrent detection on InAs wires by conductive AFM. *Ultramicroscopy* 105: 137–142.

McEllistrem, M., Haase, G., Chen, D., and Hamers, R.J. 1993. Electrostatic sample-tip interactions in the scanning tunneling microscopy. *Phys. Rev. Lett.* 70: 2471–2474.

Nagahara, T., Imura, K., and Okamoto. H. 2004. Time-resolved scanning near-field optical microscopy with supercontinuum light pulses generated in microstructure fiber. *Rev. Sci. Instrum.* 75: 4528–4533.

Naruse, N., Mera, Y., Fukuzawa, Y., Nakamura, Y., Ichikawa, M., and Maeda, K. 2007. Fourier transform photoabsorption spectroscopy based on scanning tunneling microscopy. *J. Appl. Phys.* 102: 114301.

Nechay, B.A., Siegner, U., Achermann, M., Bielefeldt, H., and Keller, U. 1999. Femtosecond pump-probe near-field optical microscopy. *Rev. Sci. Instrum.* 70: 2758–2764.

Novotny, L., Pohl, D., and Hecht, B. 1995. Scanning near-field optical probe with ultrasmall spot size. *Opt. Lett.* 20: 970–972.

Othonos, A. 1998. Probing ultrafast carrier and phonon dynamics in semiconductors. *J. Appl. Phys.* 83: 1789–1830.

Pierce, D.T. and Meier, F. 1976. Photoemission of spin-polarized electrons from GaAs. *Phys. Rev. B* 13: 5484–5500.

Pohl, D.W. 1984. Optical stethoscopy: Image recording with resolution λ/20. *Appl. Phys. Lett.* 44: 651–653.

Prins, M.W.J., Jansen, R., Groeneveld, R.H.M., van Gelder, A.P., and van Kempen, H. 1996. Photoelectrical properties of semiconductor tips in scanning tunneling microscopy. *Phys. Rev. B* 53: 8090–8104.

Qiu, X.H. 2003. Vibrationally resolved fluorescence excited with submolecular precision. *Science* 299: 542–546.

Saito, A., Maruyama, J., Manabe, K., Kitamoto, K., Takahashi, K., Takami, K., Yabashi, M., and Tanaka, Y. 2006. Development of a scanning tunneling microscope for in situ experiments with a synchrotron radiation hard-x-ray microbeam. *J. Synchrotron Rad.* 13: 216–20.

Sakurai, M. 2004. Optical selection rules in light emission from the scanning tunneling microscope. *Phys. Rev. Lett.* 93: 046102-1–4.

Sakurai, T. and Watanabe, Y. 1999. *Advances in Scanning Probe Microscopy*. Springer, New York.

Shah, J. 1999. *Ultrafast Spectroscopy of Semiconductors and Semiconductor Nanostructures*. Springer, Berlin, Germany.

Shigekawa, H., Takeuchi, O., and Aoyama, M. 2005. Development of femtosecond time-resolved scanning tunneling microscopy for nanoscale science and technology. *Sci. Technol. Adv. Mater.* 6: 582–588.

Shigekawa, H., Yoshida, S., Takeuchi, O., and Terada, Y. 2008. Nanoscale dynamics probed by laser-combined scanning tunneling microscopy. *Thin Solid Films* 516: 2348–2357.

Sommerhalter, C., Matthes, T.W., and Boneberg, J. 1997. Tunneling spectroscopy on semiconductors with a low surface state density. *J. Vac. Sci. Technol. B* 15: 1876–1883.

Suzuki, Y. 1997. Magnetic domains of cobalt ultrathin films observed with a scanning tunneling microscope using optically pumped GaAs tips. *Appl. Phys. Lett.* 71: 3153–3155.

Takeuchi, O., Yoshida, S., and Shigekawa, H. 2004a. Light-modulated scanning tunneling spectroscopy for nanoscale imaging of surface photovoltage. *Appl. Phys. Lett.* 84: 3645–3647.

Takeuchi, O., Aoyama, M., Oshima, R., Okada, Y., Oigawa, H., Sano, N., Morita, R. et al. 2004b. Probing subpicosecond dynamics using pulsed laser combined scanning tunneling microscopy. *Appl. Phys. Lett.* 85: 3268–3270.

Terada, Y., Takeuchi, O., Shigekawa, H., Aoyama, M., Kondo, H., and Taninaka, A. 2007. Ultrafast photoinduced carrier dynamics in GaNAs probed using femtosecond time-resolved scanning tunneling microscopy. *Nanotechnology* 18: 044028.

Terada, Y., Yoshida, S., Okubo, A., Kanazawa, K., Xu, M., Takeuchi, O., and Shigekawa, H. 2008. Optical doping: Active control of metal-insulator transition in nanowire. *Nano Lett.* 8: 3577–3581.

Terada, Y., Yoshida, S., Takeuchi, O., Shigekawa, H. et al. 2010. Imaging ultrafast carrier dynamics in nanoscale potential landscapes by femtosecond time-resolved scanning tunneling microscopy, in press.

Tortonese, M. 1991. Atomic force microscopy using a piezoresistive cantilever. *International Conference on Solid-State Sensors and Actuators*, Pennington, NJ, IEEE Publication 91CH2817-5, pp. 448–451.

Wang, X. 2005. Large-scale molecular dynamics simulation of surface nanostructuring with a laser-assisted scanning tunnelling microscope. *J. Phys. D: Appl. Phys.* 38: 1805–1823.

Wiesendanger, R. 1994. *Scanning Probe Microscopy and Spectroscopy*. Cambridge University Press, Cambridge, U.K.

Williams, C. 2008. Fabrication of gold tips suitable for tip-enhanced Raman spectroscopy. *J. Vac. Sci. Technol. B* 26: 1761–1764.

Yamashita, M., Shigekawa, H., and Morita, R. 2005. *Mono-Cycle Photonics and Optical Scanning Tunneling Microscopy—Route to Femtosecond Angstrom Technology*. Springer, Berlin, Germany.

Yasuda, S., Nakamura, T., Matsumoto, M., and Shigekawa, H. 2003. Phase switching of a single isomeric molecule and associated characteristic rectification. *J. Am. Chem. Soc.* 125: 16430–16433.

Yoshida, S., Takeuchi, O., Shigekawa, H., Kikuchi, J., Kanitani, Y., and Oigawa, H. 2006. Tip-induced band bending and its effect on local barrier height measurement studied by light modulated scanning tunneling spectroscopy. *Surf. Sci. Technol.* 4: 192–196 (e-journal).

Yoshida, S., Takeuchi, O., Shigekawa, H., Kanitani, Y., Oshima, R., and Okada, Y. 2007. Microscopic basis for the mechanism of carrier dynamics in an operating p-n junction examined by using light-modulated scanning tunneling spectroscopy. *Phys. Rev. Lett.* 98: 026802–026805.

Yoshida, S., Kanitani, Y., Takeuchi, O., and Shigekawa, H. 2008. Probing nanoscale potential modulation by defect-induced gap states on GaAs(110) using light-modulated scanning tunneling spectroscopy. *Appl. Phys. Lett.* 92: 102105–102107.